Supporting Information (SI)

A Z-Scheme BiOCl/UiO-66(Zr/Ti) Heterojunction with Engineered Interfacial Contacts for Synergistic Pollutant Mineralization and Selective Sulfoxidation

Wentao Wu [a], Xingxing Wu[b], Chen kai Peng [a], Yang Zhao[c], Danxia Zhao [a] *

[a]*Institute of Environmental Engineering Technology, School of Life Sciences, Taizhou University, Taizhou 318000, Zhejiang, P.R. China*

[b] *Taizhou Pollution Control Technology Centre Co, LTD, Taizhou, Zhejiang, 310012, China.*

[c] *Zhengzhou Health Vocational College, Zhengzhou, Henan, 450100, China.*

* co-corresponding author: Tel: +86 18362098479 E-mail address: danxia@tzc.edu.cn

Experimental

Materials

All commercial chemicals and analytical grade solvents are supplied by Shanghai Macklin Biochemical Co. Ltd and can be used without further purification.

Preparation of UiO-66(Zr) and BiOCl/UiO-66(Zr)

$ZrCl_4$ (6.65 mmol), an excess terephthalic acid (BDC) (10.11 mmol), HCl 37 % solution (1 mL) and N, N-dimethylformamide (DMF) (200 mL) were put into a glass flask and stirred continuously for 10 min. Then transfer the mixture to a 250 mL hydrothermal reaction vessel and incubate it in a 130°C convection drying oven for 24 h. The obtained white precipitate was washed with DMF (3 × 50 mL) and ethanol (3 × 50 mL), and finally activate the sample by heating it in a vacuum drying oven at 80°C for 24 hours [1]. Under the same conditions, BiOCl/UiO-66 (Zr) was prepared by replacing UiO-66(Zr/Ti) with UiO-66(Zr), and the sample was labeled as BZ.

Characterization of photocatalysts

The X-ray diffractometry (XRD) using a Shimadzu XRD-6000 diffractometer with Cu Kα irradiation. The specific surface area of samples was calculated using Brunauer-Emmett-Teller (BET) method and the pore-size distribution was assessed by the sorption/desorption isotherms of N2 employing Barrett-Joyner-Halenda (BJH) equation on TreStar 3020. The scanning electron microscopy (SEM) images was performed using a Hitachi S-4800. TEM images were taken using a PHILIPS Tecnai 12 microscope operating at 120 kv. Energy Dispersive X-ray Spectroscopic analysis (EDS) was performed with a JEM-2010(HR) transmission electron microscope at an acceleration voltage of 200kV. High Resolution Transmission electron microscopy (HRTEM) was performed on Philips-FEI Tecnai G2 F20 operating at 300kv. The specific surface areas were calculated using the Brunauer-Emmett-Teller (BET) method. In addition, the

XPS measurements were carried out on an ESCALAB 250Xi spectrometer (Thermo Scientific, USA) in dark conditions. All samples were analyzed under a pressure of less than 1.0×10^{-9} Pa. Spectra were acquired through the avantage software (Version 5.979) with a step of 0.05 eV. The UV-Vis diffuse reflectance spectra (UV-vis DRS) of the catalysts were recorded on a UV-Vis spectrometer (Lambda 750) within the range of 200 - 1100 nm. Photoluminescence spectra (PL) of the catalysts were carried out on a spectrophotometer (LabRAM HR Evolution). Contact potential difference (CPD) was measured on a kelvin probe apparatus (Instytut Fotonowy, Poland). And the work function of the probe is calibrated to be 4.25 eV by the highly oriented pyrolytic graphite as a standard reference surface. Ultraviolet photoelectron spectroscopy (UPS) measurements were acquired using a Thermo Fisher Nexsa. A He-Iα lamp ($h\nu$ = 21.22 eV) was used as the radiation source and the samples were kept under -5 V bias during the measurement. X-ray absorption fine structure spectroscopy (XAFS) at the Zr K-edge, and Ti K-edge (transmission mode) was operated at the beamline BL11B of SSRF (Shanghai Synchrotron Radiation Facility), Shanghai Institute of Applied Physics, Chinese Academy of Sciences (CAS).

Photocatalytic degradation experiments

Photocatalytic degradation of RhB by BZT in different water matrices under visible LED irradiation. Water samples: deionized water (D.I.), Xinhu Lake water (from Taizhou University campus, Taizhou), and Yongning River water (from Jiaojiang District, Taizhou). All natural water samples were filtered through a 0.45 μm membrane before use. Initial RhB concentration: 100 $mg \cdot L^{-1}$; catalyst dosage: 10 mg in 50 mL solution. The intermediates produced in the photodegradation process of RhB were identified by high performance liquid chromatography-mass spectrometry (LC/MS). Mobile phase was a mixture of 5 acetonitrile and formic acid (0.1%) with a flow rate of 0.25 mL/min. The injection volume was 5.0 μL. The fragment voltage was 135 V and the capillary voltage was 2800 V. The mass range of the MS is m/z 100-600. The total organic carbon content (TOC) and mineralization during the photocatalytic degradation process were measured using a Shimadzu TOC-V total organic carbon analyzer (Shimadzu, Japan).

The degradation rate R was estimated according to the following equation:

$$R\ (\%) = [(C_0\text{-}C_t)/C_0]\times 100\% \quad (S1)$$

The rate constant K was calculated according to the pseudo-first kinetics equation as follows:

$$K= -\ln(C_t/C_0)/t \quad (S2)$$

where C_0 and C_t denote the RhB concentration at the starting time and after irradiating, respectively.

Oxidation experiment of methyl phenyl sulfide (MPS): a 25 mL glass vial was employed as the reaction vessel. Initially, 10 mg of photocatalyst and 0.3 mmol of MPS were dissolved in 5 mL of a mixed solvent (H_2O:CH_3CN = 1:3, v/v) under continuous magnetic stirring. After stirring for 0.5 h, the vial was sealed under an O_2 atmosphere and irradiated at room temperature with a 100 W UV light positioned 10 cm away from the side of the reaction vessel for 1.5 h. Upon completion of the reaction, the resulting mixture was extracted with ethyl acetate to separate the organic phase from the aqueous phase. The conversion and selectivity were determined by gas chromatography-mass spectrometry (GC-MS). The spent catalyst was recovered via centrifugation, washed four times with deionized water and ethanol, dried, and subsequently reused for the next catalytic cycle.

Photocatalytic oxidation of methyl phenyl sulfide (MPS)

The conversion of MPS was calculated as:

$$\text{Con. } (\%) = [(C_0^{MPS} - C_t^{MPS}/C_0^{MPS})] \times 100\% \quad (S3)$$

where C_0^{MPS} and C_t^{MPS} represent the initial concentration and the concentration at time *t* of MPS, respectively.

The selectivity Methyl Phenyl Sulfoxide (MPSO) formation was defined as:

$$S_{MPSO}\ (\%) = [C_t^{MPSO}/(C_t^{MPS} - C_t^{MPS})] \times 100\% \quad \text{(S4)}$$

where C_t^{MPSO} is the concentration of MPSO at time *t*, and the denominator accounts for the total consumed MPS.

Degradation turnover

The degradation turnover number (TON) is calculated based on the mass of the catalyst (mg), reaction time (h), and pollutant concentration (μg/L) [2].

$$TON = \frac{(C_0 - C_{final}) \times V}{m_{catalyst} \times t} \quad \text{(S5)}$$

where C_0 and C_{final} are the pollutant concentrations (μg/L) before and after the reaction, $m_{catalyst}$ is the mass (mg) of the solid catalyst used, t is the reaction time (h), and V is the volume (L) of the solution.

Band structure analysis

The band gaps (E_g) of the samples were calculated by applying the subsequent equation (Eq. (S6))[3]:

$$(\alpha h\nu)^N = A(h\nu - E_g) \quad \text{(S6)}$$

where α denoted the absorption coefficient, *h* signified the Planck constant, *v* represented the frequency of the photon, A was a proportionality constant, and E_g referred to the optical bandgap. Additionally, the index N was defined as N = 1/2 for indirect bandgap semiconductors and N = 2 for direct bandgap semiconductors, elucidating the characteristics of the electronic transitions occurring within the materials. Moreover, the EVB, NHE positions of the semiconductors were determined using the following formula (Eq. (S7)):

$$E_{VB,\ NHE} = \varphi + E_{VB,\ XPS} - 4.44 \quad \text{(S7)}$$

where $E_{VB,\ NHE}$ denoted the valence band potential associated with the normal hydrogen electrode (NHE), φ signified the working function of the instrument, and the value of 4.44 eV was utilized to calibrate the discrepancy between the results obtained from XPS measurements and the reference potential of the NHE.

Influence of Environmental Factors on Photocatalytic Activity

The effects of different ions on RhB degradation were investigated; 5 mM Cl^-, SO_4^{2-}, HPO_4^{2-}, HCO_3^-, Ca^{2+} and K^+ were added to the system. In addition, the pH of the initial RhB solution was adjusted using NaOH and H_2SO_4 solutions.

Cyclic experiment

In each cycle of the photocatalytic reaction, the used BZT was collected and rinsed, and then dried overnight. The obtained sample was reintroduced into a new reaction system for cyclic experiments to determine the reusability of BZT.

Free radical trapping experiments

Free radical trapping experiments were conducted based on the above experimental procedures, using 5 mM ethylenediaminetetraacetic acid disodium salt (EDTA-2Na), Na_3N, isopropanol (IPA), and benzoquinone (BQ) as scavengers for photogenerated holes, singlet oxygen, hydroxyl radicals, and superoxide radicals, respectively.

Electrochemical measurements

Electrochemical and photoelectrochemical measurements were carried out on an electrochemical workstation (CHI 660E, Shanghai) with a standard three-electrode system. The powder coated on indium-tin-oxide (ITO) glass substrate was applied as the working electrode. 10 mg powder was suspended into 1

mL absolute ethanol and then the slurry was dropwise added on a ITO substrate (15 mm × 30 mm). The working electrode was exposed to air for 10 h to remove the ethanol. Platinum wire and Ag/AgCl electrode were used as the counter electrode and reference electrode, respectively. The electrolyte was 0.1 M Na_2SO_4 solution and illumination source was a 300 W Xe lamp providing simulated solar light.

EPR measurements

EPR spectra using TEMP as a trapping agent were recorded using a Wilmad WG-810-A quartz flat cell in a mixture of O_2^-substrated H_2O/MeOH (1:4 v/v) of BCT (4 mg mL^{-1}) and TEMP (1.2 M). ESR spectra utilizing DMPO as a trapping agent were recorded using a Wilmad WG-810-A quartz flat cell in a mixture in O_2^-substrated H_2O/MeOH (1:4 v/v) of BZT (4 mg mL^{-1}) and DMPO (1.8 M). ESR analysis was carried out at microwave frequency of 9.21 GHz at 298 K in the dark or under visible light ($\lambda > 420$ nm).

Computational methodologies and models

All the calculations are performed in the framework of the density functional theory with the projector augmented plane-wave method, as implemented in the Vienna ab initio simulation package [4]. The generalized gradient approximation proposed by Perdew-Burke-Ernzerhof (PBE) is selected for the exchange-correlation potential [5]. The cut-off energy for plane wave is set to 480 eV. The energy criterion is set to 10^{-4} eV in the iterative solution of the Kohn-Sham equation. All the structures are relaxed until the residual forces on the atoms have declined to less than 0.02 eV/Å. To avoid interlaminar interactions, a vacuum spacing of 20 Å is applied perpendicular to the slab. Here, we define $\Delta\rho = \rho_{BiOCl/MOF} - \rho_{BiOCl} - \rho_{MOF}$ as the charge density difference of BiOCl/MOF heterostructure, where $\rho_{BiOCl/MOF}$, ρ_{BiOCl} and ρ_{MOF} are the charge densities of BiOCl/MOF heterostructure, isolated BiOCl and MOF slabs, respectively. We use the Bader charge to express the charge transfer quantity.

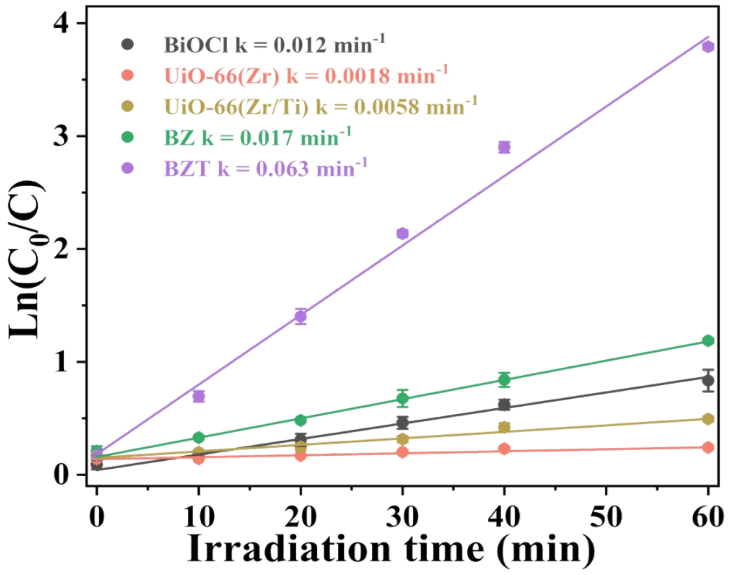

Figure S1. The rate constants of RhB degradation by different catalysts.

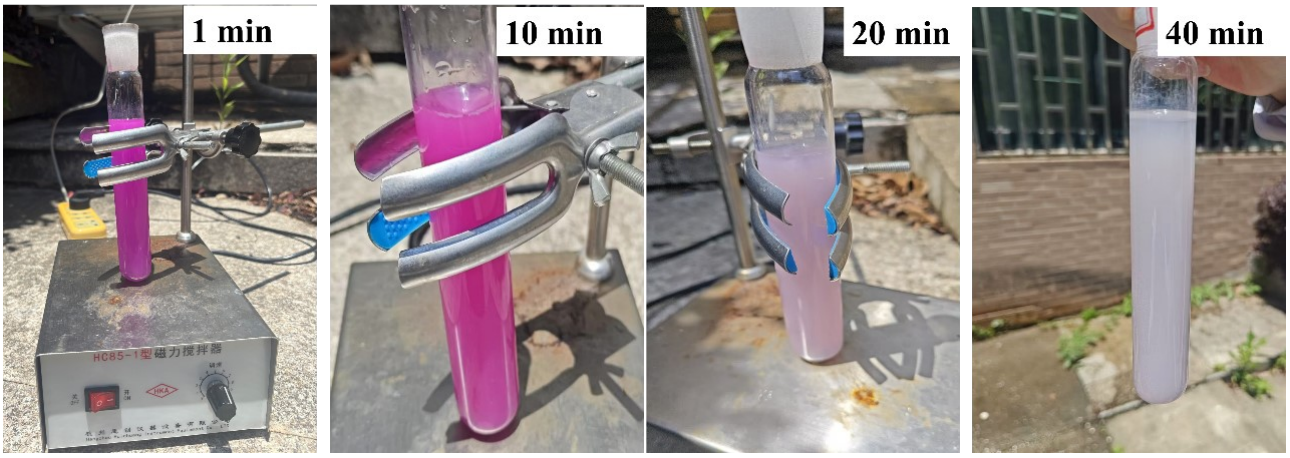

Figure S2. The results of the photocatalytic degradation of RhB by BZT under natural sunlight.

On May 15, 2025, we conducted an experiment on the photocatalytic degradation of RhB by BZT in natural sunlight in Taizhou. The reaction took place from 9:30 to 10:30, during which the reactor was exposed to direct sunlight at temperatures ranging from 25 to 30 ℃. Due to weather conditions, the other catalysts BiOCl, UiO-66(Zr), UiO-66(Zr/Ti), and BZ were subsequently tested on May 28 to 30 from 9:30 to 10:30, with an exposure temperature of 26 ± 5 ℃.

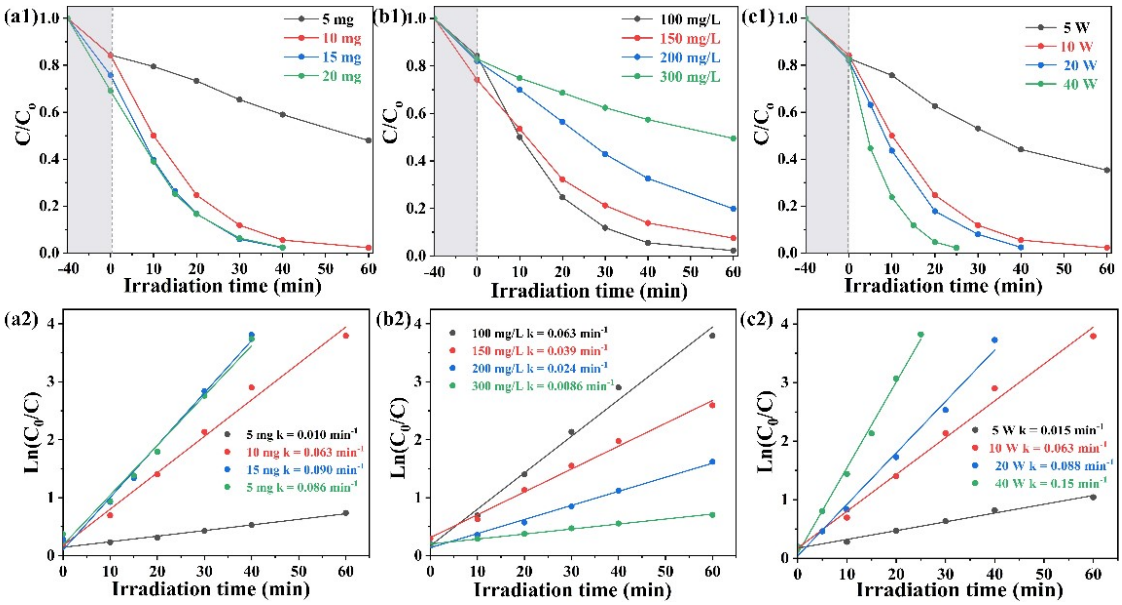

Figure S3. (a1, a2) different catalysts; (b1, b2) different RhB concentrations; (c1, c2) different powers affecting RhB photodegradation.

The effects of catalyst dosage and pollutant concentration were systematically studied. An optimal dosage of 15 mg BZT resulted in peak performance, with no significant gain beyond this threshold (Figure S3a). Similarly, RhB degradation efficiency declined at initial concentrations above 200 $mg \cdot L^{-1}$ due to saturation of active sites (Figure S3b). These results suggest that BZT remains effective across a broad pollutant concentration range and maintains high catalytic activity under ultra-low power densities, making it suitable for real-world, low-light environmental conditions such as indoor or overcast settings. Notably, efficient degradation was maintained under LED sources: 65 % removal at 5 W and full degradation within 30 min at 40 W, with a maximum reaction rate constant of 0.15 min^{-1} (Figure S3c).

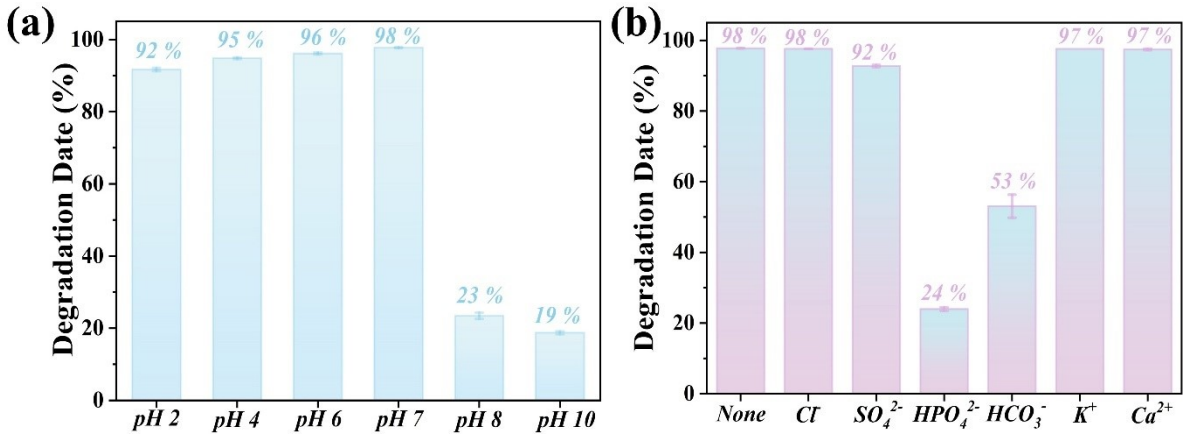

Figure S4 (a) Different pH. (b) Different ions.

To assess the environmental robustness of the BZT photocatalyst, we systematically investigated the effects of initial solution pH and common coexisting ions on RhB degradation performance under 10 W LED irradiation. As depicted in Figure S4a, the photocatalytic efficiency exhibited a strong dependence on pH. BZT maintained high activity (≥ 90 %) under acidic to neutral conditions (pH ≤ 7), while the degradation rate dropped sharply to < 25% in alkaline media. This trend is attributed to changes in the charge state of RhB: at pH ≤ 7, RhB primarily exists in a cationic form (RhB^+), which is electrostatically attracted to the negatively charged catalyst surface, promoting adsorption and degradation. Conversely, under basic conditions, RhB likely exists as a neutral or negatively charged species (RhB^0 or RhB^-), resulting in electrostatic repulsion and lower adsorption affinity. Moreover, alkaline pH may suppress the generation or stability of key reactive oxygen species (ROS), such as ·OH and $\cdot O_2^-$, thus reducing photocatalytic efficiency. The influence of coexisting ions, including Cl^-, SO_4^{2-}, HCO_3^-, HPO_4^{2-}, K^+, and Ca^{2+}, was also examined (Figure S4b). Inert cations (K^+, Ca^{2+}) and common anions (Cl^-, SO_4^{2-}) exhibited negligible interference, likely due to their weak interaction with either RhB or the catalyst surface. In contrast, HCO_3^- and HPO_4^{2-} showed notable inhibitory effects, particularly HPO_4^{2-}, which reduced the RhB removal rate to 24 %.The inhibition is attributed to two factors: (1) Competitive adsorption-polyvalent anions like HCO_3^- and HPO_4^{2-} can occupy surface active sites, hindering RhB adsorption and ROS generation; (2) Complexation with metal centers- HPO_4^{2-} may coordinate with surface Zr^{4+} and Ti^{4+} nodes to form stable

phosphate complexes (e.g., $Zr(HPO_4)_2$, $Ti(HPO_4)_2$), leading to site passivation and loss of catalytic activity. These results collectively demonstrate that the BZT catalyst exhibits excellent pH tolerance and ionic stability, especially in realistic water matrices, reinforcing its potential for practical wastewater treatment applications.

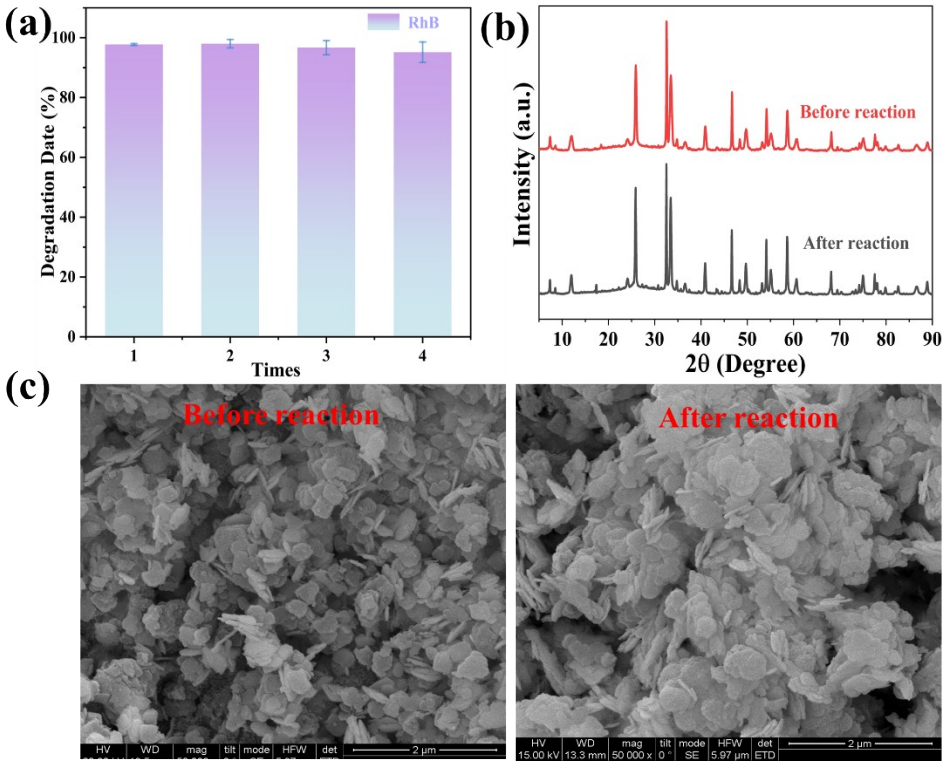

Figure S5. (a,b) Cyclic experiments of BZT degradation of RhB; (b) XRD, (c) and SEM of BZT before and after the photocatalytic reaction.

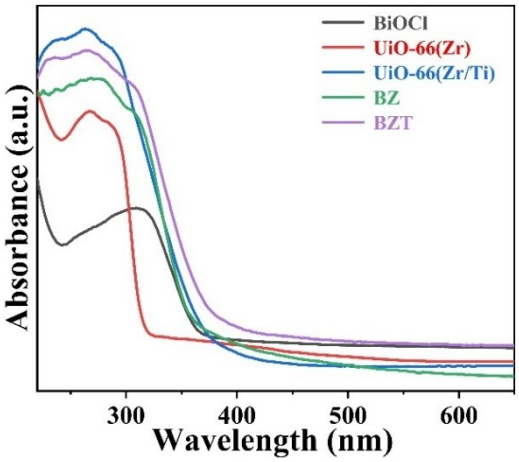

Figure S6. UV-vis DRS spectra of prepared samples.

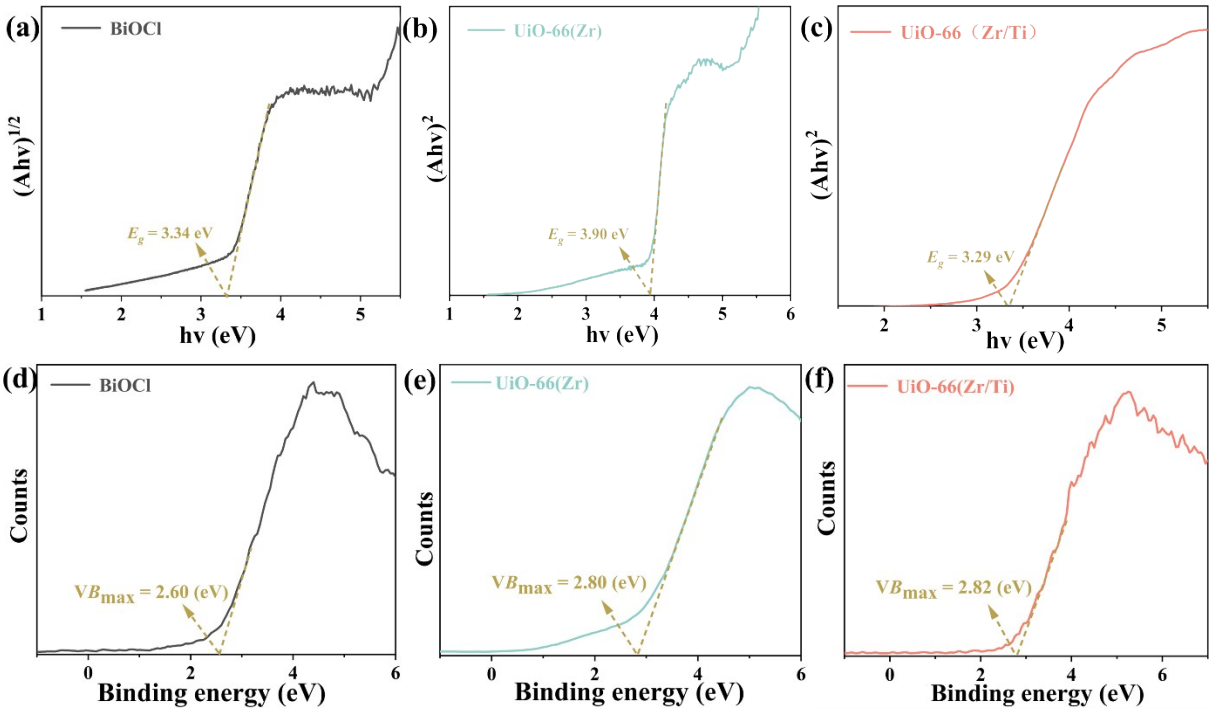

Figure S7. (a-c) plots of $(\alpha h\nu)^{1/2}$ or $(\alpha h\nu)^2$ vs $(h\nu)$ for the band gap energy of the samples calculated using the Kubelka-Munk function formul, (d-f) XPS-VB spectra of the samples.

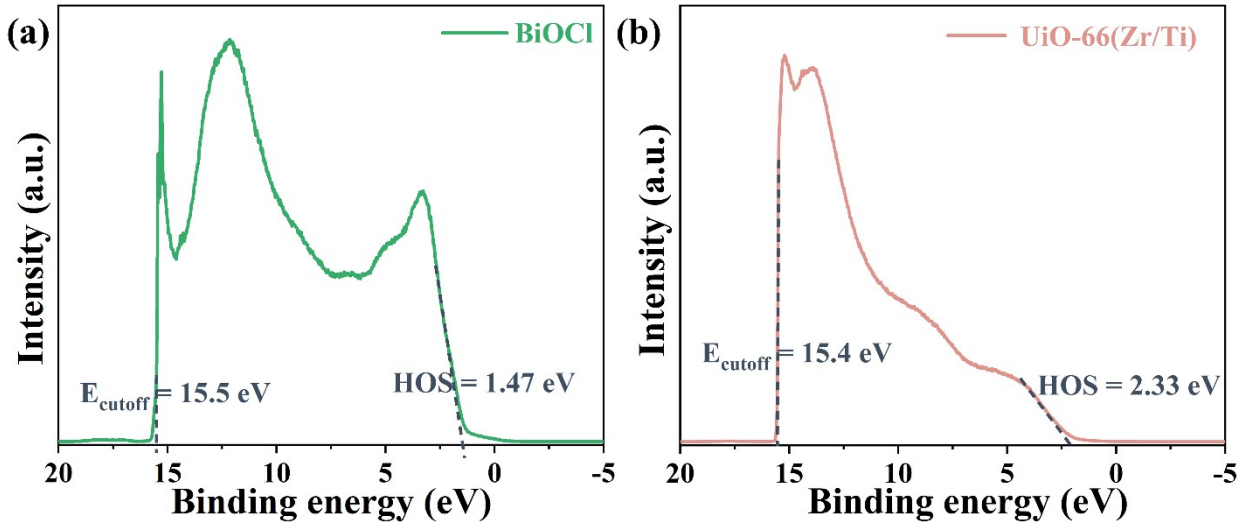

Figure S8. UPS spectra of BiOCl and UiO-66(Zr/Ti). According to the values of cutoff and the highest occupied states (HOS), ionization potential (*IP*, equivalent to valance band vs. Vacuum) could be obtained with the equation of $IP = 21.22\ eV - (E_{cutoff} - HOS)$.

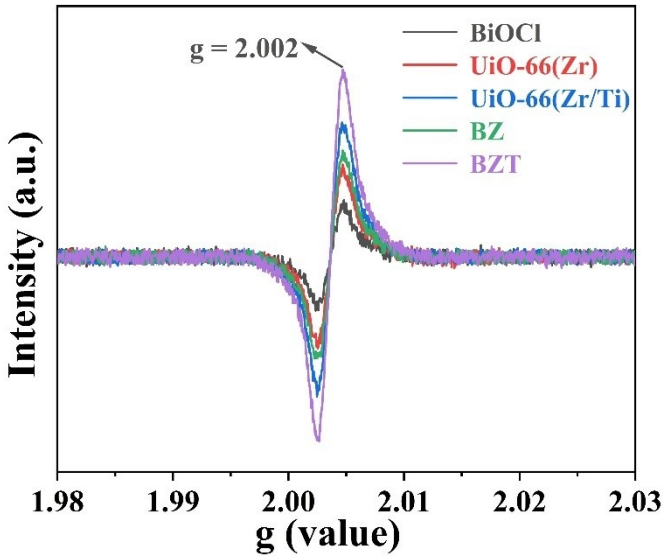

Figure S9. EPR spectra of prepared samples.

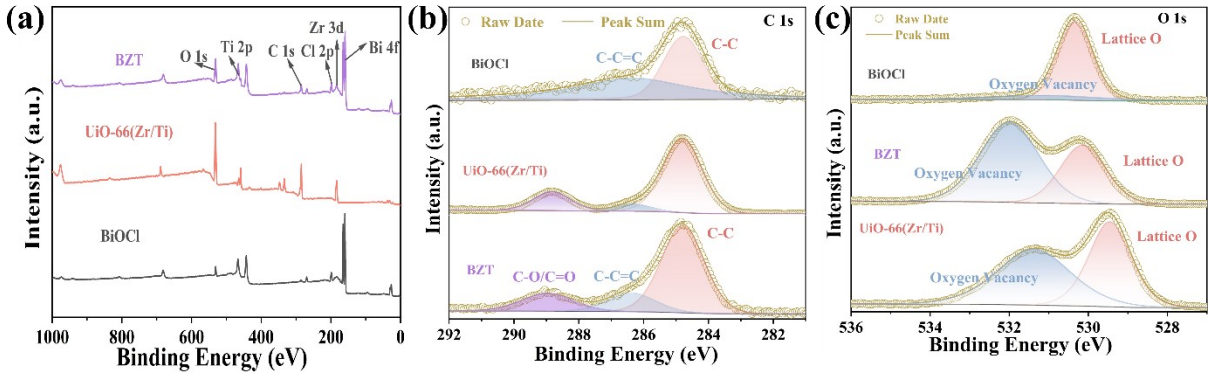

Figure S10. (a) XPS spectra of full spectra analysis of samples, (b) C 1s, and (c) O 1s of samples.

In the high-resolution C 1s spectrum (**Figure S10b**), three distinct peaks were observed at approximately 284.8, 286.3, and 288.8 eV, which can be attributed to sp^3 C–C bonds from amorphous carbon or aliphatic chains, sp^2 C=C bonds from conjugated carbon systems, and oxygen-containing groups such as C–O/C=O, respectively. Similarly, the high-resolution O 1s spectrum (**Figure S10c**) exhibits two major peaks at 530.3 and 531.4 eV, corresponding to lattice oxygen and oxygen vacancy-related species, respectively[6].

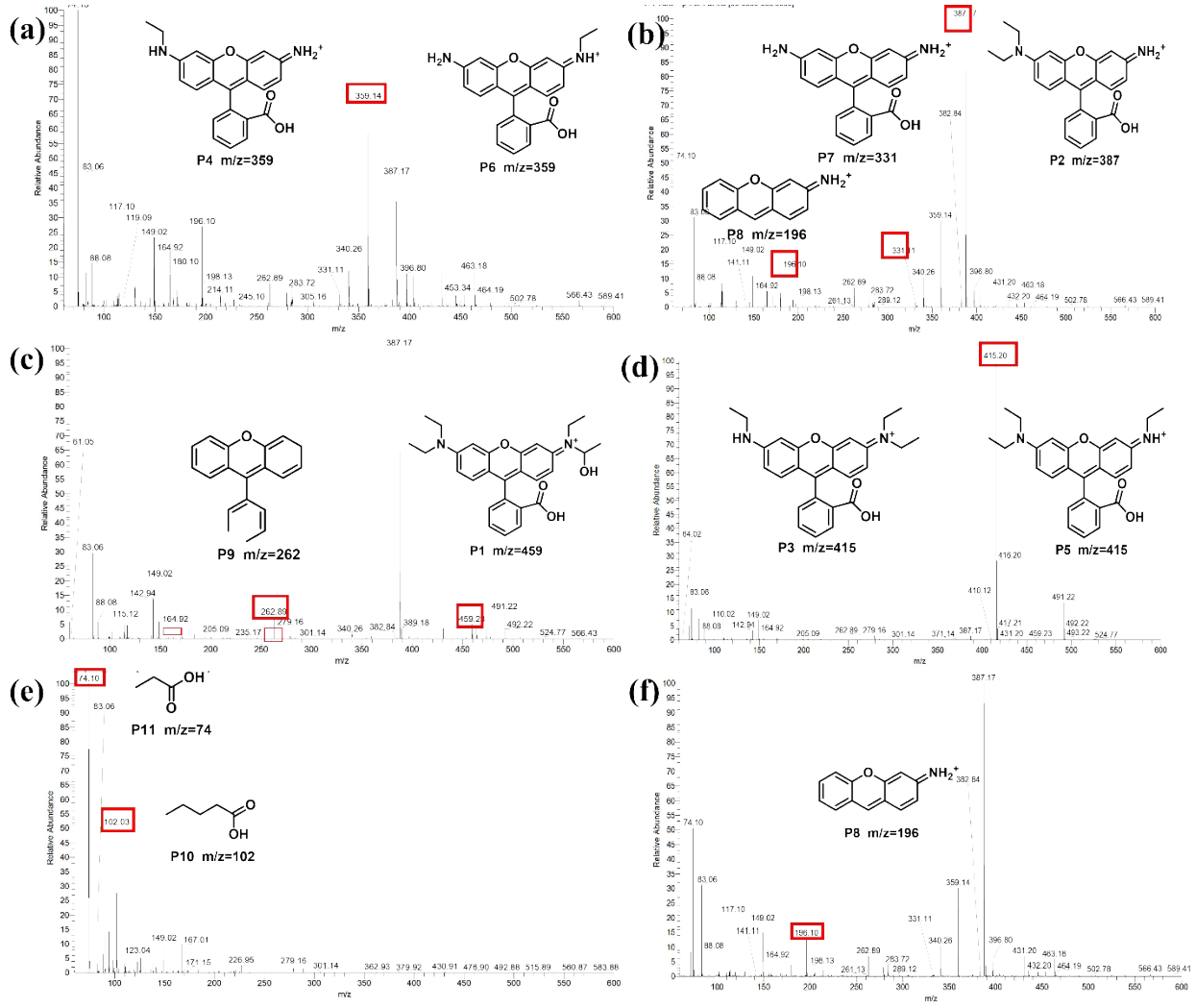

Figure S11. LC-MS spectrum of RhB and degradation intermediates under visible light irradiation: (a) 10 min, (b) 20 min, (c) 30 min, (d) 40 min, (e) 50 min, (f) 60 min.

Proposed RhB Degradation Pathway

To elucidate the degradation process of Rhodamine B (RhB) under low-power LED illumination, liquid chromatography-mass spectrometry (LC-MS) analysis was conducted after photocatalysis using BZT (**Figure S11**). The major intermediate species identified allowed for the reconstruction of a plausible stepwise degradation pathway, as shown in **Figure 6i**. The degradation begins with a stepwise N-deethylation process, in which RhB (m/z = 443) is gradually converted to N,N,N'-triethylated (m/z = 415), diethylated (m/z = 387), monoethylated (m/z = 359), and ultimately non-ethylated rhodamine (m/z = 331)[7,

8]. This sequence reflects the selective cleavage of the C-N bonds, likely facilitated by $\cdot O_2^-$ attack at the amino groups. Subsequently, the xanthene chromophore is disrupted via aromatic ring opening and hydroxylation, yielding low-molecular-weight fragments such as m/z = 262, 196, 103, and 74. These products suggest further non-selective oxidation steps involving hydroxyl radicals (·OH) and singlet oxygen $^1O_2$)[9, 10]. Taken together, the RhB degradation pathway involves: (i) Successive N-deethylation, (ii) Chromophore ring cleavage, (iii) Hydroxylation and decarboxylation, and (iv) Complete mineralization to $CO_2$and H_2O. This transformation is mainly driven by $\cdot O_2^-$ and supported by ·OH and $^1O_2$ as secondary reactive oxygen species (ROS), in line with EPR and scavenger test results.

To evaluate the environmental safety and biocompatibility of the photocatalytically treated RhB wastewater, a seed germination test using pea (Pisum sativum) was conducted under natural conditions with three different irrigation sources: deionized water (control), untreated RhB solution, and BZT-treated RhB solution. As shown in **Figure 6j**, seeds irrigated with the untreated RhB solution exhibited severe germination inhibition, with almost no sprouting observed. In contrast, the seeds exposed to photocatalytically treated RhB water-especially after 60 minutes of LED irradiation-demonstrated healthy and uniform germination, comparable to the control group. These observations suggest that the residual organics and intermediate products remaining after BZT-catalyzed photocatalytic degradation are largely non-toxic, posing negligible phytotoxicity to plants. Therefore, the treated effluent is not only decolorized and mineralized effectively but also environmentally benign, underscoring its potential for safe reuse in agricultural or ecological applications.

Table S1. The average pore diameter, specific surface area, and pore volume of the prepared sample.

Sample	S_{BET} (m^2/g)	Average pore size (nm)	Pore volume (cm^3/g)
BiOCl	14.768	18.845	0.052
UiO-66(Zr/Ti)	827.198	4.768	0.409
BZT	229.491	9.678	0.248

Table S2. Comparison of the removal ability of heterojunction catalysts for RhB.

Photocatalyst	**Dosage** (mg)	**Volume** (mL)	**RhB** (mg/L)	**Irradiation** time(h)	**Dr** (%)	**TON**	**Light source** (visible light)	**Energy Consumption**(J)	**Ref**
BiOCl/Bi-MOF	5	50	10	0.3	99	330	Xenon lamp 350 W	3.78×10^5	[11]
BiOCl/(Zn/Ti) LDH	20	40	30	2	96.3	28.9	Xenon lamp (300 W)	2.16×10^6	[12]
BiOCl/$BiVO_4$	50	100	10	0.9	99.5	22.1	Xenon lamp (300 W)	9.72×10^5	[13]
BiOCl/KTO	50	100	10	1.5	100	13.3	Xenon lamp (500 W)	2.7×10^6	[14]
Bi/P–BiOCl	50	100	20	0.5	97.3	77.8	Xenon lamp (300 W)	5.4×10^5	[15]
PANI/BiOCl/GO	12	20	5	2	96	4	Philips lamp (45w)	3.24×10^5	[16]
S-BiOCl/TaON/Bi_2O_3	10	50	5	0.4	98	61.3	Xenon lamp (300 W)	4.32×10^5	[17]
Cd/Zr-UiO-66	10	100	20	1.7	95.82	112	Xenon lamp (252 W)	1.54×10^6	[18]
UiO-66/BiOBr	100	50	10	0.7	97	6.9	Xenon lamp (300 W)	7.56×10^5	[19]
BiOCl	10	50	100	1.0	54	270	LED lamp (10W)	0.36×10^5	**This work**
UiO-66(Zr)	10	50	100	1.0	21	105	LED lamp (10W)	0.36×10^5	**This work**
UiO-66(Zr/Ti)	10	50	100	1.0	38	190	LED lamp (10W)	0.36×10^5	**This work**
BiOCl/UiO-66(Zr)	10	50	100	1.0	69	345	LED lamp (10W)	0.36×10^5	**This work**

BiOCl/UiO-66(Zr/Ti)	10	50	100	1.0	98	490	LED lamp (10W)	0.36$\mathcal{S}$ 10^5	**This work**

Notes: / means unknown, energy consumption is calculated by: W = P × T. Here, W (J) is the electrical energy consumption; P (W) is the output power of the lamp; T is the time.

Table S3. EXAFS fitting data.

	S_0^2	shell	CN*	R(Å)	σ^2	ΔE_0	R factor
Ti foil	0.95	Ti-Ti	12	2.92±0.01	0.0137	8.81±2.79	0.0055
		Ti-Ti	2	2.51±0.01	0.0078		
Ti-sample	0.95	Ti-O	4	1.97±0.01	0.0022	5.95±0.82	0.0027
		Ti-O	3.7	3.08±0.01	0.0003		
		Ti-Zr	1.8	3.51±0.01	0.0080		
Zr foil	0.98	Zr-Zr	6	3.21±0.01	0.0030	-1.01±0.60	0.0090
		Zr-Zr	6	3.34±0.01	0.0150		
Zr-sample	0.98	Zr-O	6.1	2.19±0.01	0.0057	2.42±0.40	0.0022
		Zr-O	1.2	2.79±0.01	0.0099		
		Zr-Ti	4.1	3.52±0.01	0.0106		

CN: coordination numbers; *R*: bond distance; σ^2: Debye-Waller factors; ΔE_0: the inner potential correction. R factor: goodness of fit. Error bounds that characterize the structural parameters obtained EXAFS spectroscopy were estimated as·CN±20%; R·±·1%; σ^2± 20%.

References

[1] J. Marreiros, R. de Oliveira-Silva, P. Iacomi, P. L. Llewellyn, R. Ameloot and D. Sakellariou, Benchtop In Situ Measurement of Full Adsorption Isotherms by NMR, J. Am. Chem. Soc. 143 (2021) 8249-8254.

[2] W. Zhang, Y. Wang, T. Fang, X. Tang, Z. Ding, Y. Han, R. Guo, P. Qi and X. Liu, Customization of indium-based MOFs for enhanced adsorptive and photocatalytic of organic pollutants: Morphology involvement on performance and mechanism, Chem. Eng. J. 498 (2024) 155449.

[3] Y. Ma, Y. Zhang, H. Rong, J. Pan, C. Gan, Z. Yang, Y. Guo, Y. Yuan and N. Wang, Constructing a core-shell heterojunction with photo-activated antifouling shield via interface engineering for uranium extraction from water, Desalination. 620 (2026) 119662.

[4] G. Kresse and D. Joubert, From ultrasoft pseudopotentials to the projector augmented-wave method, Phys. Rev. B. 59 (1999) 1758-1775.

[5] J. P. Perdew, K. Burke and M. Ernzerhof, Generalized Gradient Approximation Made Simple, Phys. Rev. Lett. 77 (1996) 3865-3868.

[6] M. G. Ahmed, Y. F. Tay, X. Chi, A. S. Razeen, Y. Fang, M. Zhang, A. Sng, S. Y. Chiam, A. Rusydi and L. H. Wong, Cation Migration-Induced Lattice Oxygen Oxidation in Spinel Oxide for Superior Oxygen Evolution Reaction, Angewandte Chemie International Edition. 64 (2025) e202416757.

[7] S. Geng, X. Sui, Y. Li, H. Wang, X. Zhao, L. Chang and X. Duan, Reinforcing piezo-photocatalytic properties and enhancing RhB degradation efficiency of Ce-doped Bi4Ti3O12: mechanistic insights, Journal of Materials Chemistry A. (2025)

[8] P. Xing, Y. Wang, X. Fan, X. Li, P. Wang, Q. Zhang, Q. Du, Y. Xie, R. Yin and W. Gan, Rapid Synthesis and Recycling of Carbonized Wood Catalyst Decorated with Co Nanoparticles for High-Efficiency Degradation of Rhodamine B, Advanced Functional Materials. n/a (2025) 2420933.

[9] M. Nikitha, S. S. Elanchezhiyan and S. Meenakshi, Photodegradation of rhodamine-B in aqueous environment using visible-active gC3N4@CS-MoS2 nanocomposite, Environmental Research. 238 (2023) 117032.

[10] Q. Zeng, Y. Jiang, J. Ni, J. Tang, Y. Wen, X. Fu, Q. Zhang, Z. Xiong and T. Cai, Highly efficient removing refractory organics continuously using a Fenton-like Filter: The role of in-situ galvanic effect enhanced peroxymonosulfate activation, Chemical Engineering Journal. 450 (2022) 138067.

[11] H. Shi, M. Xu, C. Leng, L. Ai, L. Wang, H. Fan and S. Wu, In situ construction of S-scheme heterojunctions between BiOCl and Bi-MOF for enhanced photocatalytic CO2 reduction and pollutant degradation, Journal of Colloid and Interface Science. 680 (2025) 1067-1078.

[12] L. Wu, X.-J. Yang, K. Ma, X. Qu, Y. Zhang, H. Xia, J. Wu, S. Lu and D. Liu, 2D/2D ultrathin (Zn/Ti)LDH/BiOCl Z-scheme heterostructure nanosheets boosted visible-light-catalytic degradation of dyes and antibiotics, Composites Part B: Engineering. 293 (2025) 112144.

[13] L. Yi, H. Jiang, Y. Ma, R. Zhu, G. Zhang and Z. Ren, Highly efficient visible-light driven dye degradation via 0D BiVO4 nanoparticles/2D BiOCl nanosheets p-n heterojunctions, Chemosphere. 354 (2024) 141658.

[14] M. Durai, D. Chauhan, M. Durai, M. Saravanan, S. Kumaravel, E. Erusappan and Y.-H. Ahn, Layered KTO/BiOCl nanostructures for the efficient visible light photocatalytic degradation of harmful dyes, Chemosphere. 306 (2022) 135659.

[15] H. Ma, Y. Wang, Z. Zhang, J. Liu, Y. Yu, S. Zuo and B. Li, A superior ternary Z-scheme photocatalyst of Bi/Black Phosphorus nanosheets/P-doped BiOCl containing interfacial P–P bond and metallic mediator for H2O2 production and RhB degradation, Chemosphere. 330 (2023) 138717.

[16] P. Hait, R. Mehta and S. Basu, Advancing sustainable solutions: Harnessing polyaniline/BiOCl/GO ternary nanocomposites for solar-powered degradation of organic pollutant and photocatalytic hydrogen generation, Journal of Cleaner Production. 424 (2023) 138851.

[17] X. Yang, S. Sun, Z. Shi, D. Yun, Y. Guo, C. Liu, B. Yang, M. Yang, Q. Yang and J. Cui, One-pot construction of highly efficient TaON/Bi2O3/S–BiOCl ternary photocatalysts: Simultaneously integrating type-I with Z-scheme junctions for improved visible light-driven removal of organic pollutants, Chemosphere. 307 (2022) 135979.

[18] W. Cheng, Y. Wang, S. Ge, X. Ding, Z. Cui and Q. Shao, One-step microwave hydrothermal preparation of Cd/Zr-bimetallic metal–organic frameworks for enhanced photochemical properties, Advanced Composites and Hybrid Materials. 4 (2021) 150-161.

[19] Z. Chen, J. Zhao, J. Chen, Y. Zhang, D. Chen, Q. Wang and D. Xia, UiO-66/BiOBr heterojunction functionalized cotton fabrics as flexible photocatalyst for visible-light driven degradation of dyes and Cr(VI), Separation and Purification Technology. 258 (2021) 118007.